



with long-term radial-velocity variations (VAR). We determined the orbital solutions of seven systems. For two hierarchical triple systems, we also proposed a preliminary solution for the outer orbit. Using the classification results, we provided a lower limit of the fraction of A/F-type hybrid pulsators which belong to spectroscopic binary and multiple systems. Including the known *Kepler* eclipsing binary KIC 11180361 (KOI-971), we derived a minimum multiplicity fraction of 27%. Two other hybrid targets have a possible companion or shell (CMP). If we count these two targets, we obtain an overall multiplicity fraction of about 30% among these candidate hybrid pulsators.

Among the new spectroscopic systems, we identified four cases for which analysis of the *Kepler* time delays (TDs) (mostly derived from the short-period pulsation frequencies) with the radial velocities (RVs) enables us to derive improved orbital elements, accurate mass ratios as well as a (most) probable identification of the pulsating component. The goal of this paper is to determine orbital solutions for these systems as accurately as possible based on the results of a unified modelling by combining the various data types into a single, simultaneous analysis. In the present study, we will make usage of the radial velocities acquired with the échelle spectrograph HERMES equipping the 1.2-m Mercator telescope, La Palma, Spain (Raskin et al. 2011) available from Paper I (see table C.2). Furthermore, we reported variable TDs in nine cases, in particular for the spectroscopic systems KIC 4480321, 5219533, 8975515, and KIC 9775454 (Paper I, fig. 24). For all four systems, our spectroscopic observations were acquired until late 2019. For KIC 9775454, we included the measurements obtained in 2018 with the high-resolution échelle spectrograph HESP (R = 60,000) mounted at the Himalayan Chandrasekhar telescope (HCT), operated by the IIA, Bangalore, India<sup>1</sup>. Consequently, all RV data of all four systems and their components were updated to the latest possible date. First, we present the current status of each individual system (Sect. 2). In Sect. 3, we introduce the methodology for computing the refined orbits. Sect. 4 provides the orbital solutions using simultaneous modelling. In Sect. 5, we present and discuss the distributions of the frequency spacings in the high-frequency region of the Fourier transforms of each system. Finally, we present our conclusions for all the treated systems (Sect. 6).

## 2. Presentation of the systems

We present a summary of useful high-resolution spectra for each of the four systems listed in Table 1. In addition to the total number of spectra available for each system, we also mention the spectrograph and the time basis. The revised orbital solutions (Sect. 4) are thus based on the combination of updated sets of component RVs and the time delays (TDs) previously derived from time-dependent frequency analyses of the oscillations detected in the *Kepler* light curves (Paper I), providing us with a total time basis longer than eight years for each case.

### 2.1. KIC 4480321

KIC 4480321 (HD 225479, V=10.3, A9 Vwkm) is a hybrid variable star revealed by Uytterhoeven et al. (2011), with frequencies in the ranges [0.2, 5.0] d<sup>-1</sup> and [5.1, 61.2] d<sup>-1</sup> and

<sup>1</sup> <https://www.iiap.res.in/hesp>

Table 1: List of targets and general properties of the RV data.

KIC ID	Nr	BJD start 2,450,000.+	BJD end 2,450,000.+	Time range (from/to)	Instr. <sup>2</sup>
4480321	61	5820.4499	8676.4431	15/09/2011 - 11/07/2019	H1
5219533	52	5372.7083	8792.3578	25/06/2010 - 04/11/2019	H1
8975515	31	5345.7088	8792.3686	29/05/2010 - 04/11/2019	H1
9775454	26	5345.7325	8794.3056	29/05/2010 - 06/11/2019	H1
9775454	2	8231.4431	8232.3771	22/04/2018 - 23/04/2018	H2

Notes. <sup>(2)</sup> H1 stands for 'HERMES'. H2 stands for 'HESP'.

a most dominant frequency of 0.710 d<sup>-1</sup> in the  $\gamma$  Dor region. The star was also reported as rotationally variable (Nielsen et al. 2013), with g-mode multiplets split by rotation. The period spacings in the  $\gamma$  Dor region were obtained by Li et al. (2019). This star was classified as an SB3 from our multi-epoch study. It is a hierarchical system, with a twin-like inner binary consisting of early F-type stars orbiting a slightly more luminous and more rapidly rotating A-type companion (we used the basic model of an A5-star,  $v \sin i = 160$  km s<sup>-1</sup> with 2 F0-stars,  $v \sin i = 10$  km s<sup>-1</sup>, Paper I). We derived an orbital solution for the inner pair with a 9.1659 d period, and an outer orbital solution with an estimated 2280 d period, and reported the existence of variable TDs in excellent agreement with the proposed solution for the outer orbit. We determined the component effective temperatures  $T_{\text{eff}1} = 7900 \pm 100$  K and  $T_{\text{eff}2}$  and  $T_{\text{eff}3}$  ranging between 6300 and 6900 K (the latter components have almost similar temperatures), assuming  $\log g = 4$  dex (cgs) (Paper I, Sect. 6.3). Murphy et al. (2018, Appendix C3) reported  $P = 2270 \pm 60$  d for the outer orbit from a modelling of Lampens et al. (2018)'s RV measurements in combination with their time delays.

### 2.2. KIC 5219533

KIC 5219533 (HD 226766, BU 1474 B, V=9.2, A2-A8, Renson & Manfroid 2009) is the visual companion of BU 1474 A at an angular separation of 65" (HD 189178, V=5.44, B5 He weak (Renson & Manfroid 2009); also a spectroscopic binary). This star was classified as a *Kepler* hybrid variable star by Uytterhoeven et al. (2011), with frequencies in the ranges [0.3, 4.6] d<sup>-1</sup> and [5.4, 29.9] d<sup>-1</sup>, and a dominant frequency of 10.285 d<sup>-1</sup> (Uytterhoeven et al. 2011, Table 3). It was recognized as a new SB3 based on the multi-epoch spectra. The system is hierarchical, consisting of an inner pair with two nearly identical stars of spectral type near A5 and a more rapidly rotating outer component of a slightly cooler type. For both components of the inner pair, the mean effective temperatures of  $T_{\text{eff}1} = 8300 \pm 100$  K and  $T_{\text{eff}2} = 8200 \pm 100$  K and projected rotational velocities of 10 km s<sup>-1</sup> were obtained coupled to the light factor  $l_1 = 0.53 \pm 0.02$ , assuming  $\log g = 4$  dex (cgs) (Paper I, Sect. 6.4). Component C has  $v \sin i$  equal to 115 km s<sup>-1</sup> Uytterhoeven et al. (2011). An orbital solution with  $P_{\text{orb}} = 31.9181$  d was derived for the inner pair, while a tentative outer orbit was proposed with  $P_{\text{orb}} \sim 1600$  d. Later on, Murphy et al. (2018, Appendix C4) studied this system using the phase modulation (PM) method (Murphy et al. 2014). They derived a very high mass function and proposed that the third body is a  $\delta$  Sct star with an orbital period longer than 1500 d. Simultaneously with Lampens et al. (2018), Catanzaro et al. (2019a,b) independently observed the system (from 2014 to 2018) with the aim to

characterize the orbits, and to perform a chemical analysis of its components. They proposed the orbital parameters based on their and Lampens et al. (2018)'s RVs ( $P_1 = 31.9187$  d,  $e_1 = 0.28$ ,  $q_1 = 1.03$  and  $P_2 = 1615$  d,  $e_2 = 0.54$ ,  $f(M_{1,2}) = 0.18$ ) which confirm the findings of Paper I. They also derived the atmospheric properties  $T_{\text{eff}}$ ,  $\log g$ , and  $v \sin i$  based on 2 spectra (obtained at max RV separation) and chemical abundances based on one spectrum (max S/N), first for two components, next with the third one included. However, they were unable to derive the chemical composition of component C (except for Mg II). They concluded that both components of the close pair are twin Am stars (with underabundances of C, O, Mg, Ca and Sc and overabundances of Na, Fe-peak elements). From the simple assumption that all the components have equal mass, they suggested that the orbits might be coplanar. All previous studies explicitly mention that more data for this multiple system are needed.

### 2.3. KIC 8975515

KIC 8975515 (HD 188538, V=9.5, A6 V:) was classified as a *Kepler* hybrid star by Uytterhoeven et al. (2011). The star shows frequencies in the ranges  $[0.3 - 4.7]$  d<sup>-1</sup> and  $[5.3 - 25.8]$  d<sup>-1</sup> of the  $\gamma$  Dor and the  $\delta$  Sct pulsation regimes respectively, with the dominant frequency of  $13.97$  d<sup>-1</sup> (Uytterhoeven et al. 2011, Table 3). Therefore, we included it among our sample of A/F-type candidate hybrid stars to be monitored spectroscopically where it was recognized as a new SB2 from the multi-epoch observations. The system consists of two A-type stars of similar temperature but with dissimilar projected rotational velocities, forming an eccentric system ( $e = 0.409 \pm 0.015$ ). From a detailed spectrum fitting using the code SYNPEC (Hubeny & Lanz 1995) and the ATLAS-9 atmosphere models (Castelli & Kurucz 2003) in order to build a suitable composite model in the spectral range  $[500-520]$  nm, the mean effective temperatures  $T_{\text{eff}1} = 7440 \pm 20$  K and  $T_{\text{eff}2} = 7380 \pm 21$  K with the light factor  $l_1$  of  $0.65 \pm 0.03$  (component A), assuming  $\log g = 4$  dex (cgs), were obtained. The mean projected rotation velocities were consistently determined as  $162 \pm 2$  and  $32 \pm 1$  km s<sup>-1</sup> (Paper I, Sect. 6.12). Lampens et al. (2018) proposed a preliminary orbit with a period of the order of 1600 d, in line with the TD curve, while Murphy et al. (2018, Appendix C12) obtained a solution with a shorter period of 1090 d, using the published RVs in combination with their time delays (TDs). They furthermore assumed that the narrow-lined component is the  $\delta$  Scuti pulsator and reported a slight aperiodicity in their derived TDs.

An extensive study of its pulsational properties was recently published by Samadi-Ghadim et al. (2020). They concluded that both components are pulsating, the fast-rotating component is a pulsating hybrid star also showing retrograde r modes, while the more slowly-rotating component is a  $\delta$  Scuti pulsator.

### 2.4. KIC 9775454

KIC 9775454 (HD 185115, V=8.2, F1 Vs) is a candidate hybrid variable star from Uytterhoeven et al. (2011), with frequencies in the ranges  $[0.2, 4.6]$  d<sup>-1</sup> and  $[14.7, 14.9]$  d<sup>-1</sup> and a dominant frequency of  $4.161$  d<sup>-1</sup>. It has a Gaia DR2 RV of  $-20.22 \pm 1.02$  km s<sup>-1</sup> (Gaia Collaboration 2018). The atmospheric parameters derived from high-resolution spectroscopy are  $T_{\text{eff}} = 7287$  K and  $\log g = 4.25$  dex (cgs) with a projected rotation velocity

of  $v \sin i = 65$  km s<sup>-1</sup> (Paper I, Table C.1). Lampens et al. (2018) classified this object as a long-term SB1 of unknown orbital period. The cross-correlation function (CCF) of the composite spectrum shows a broad-lined component blended with a narrow-lined component. Murphy et al. (2018, Appendix C14) proposed an orbit with  $P_{\text{orb}} = 1686 \pm 13$  d and  $e = 0.23 \pm 0.02$  by combining the published RVs with their TDs. In this case, the secondary component contributes only weakly to the composite spectrum. Nevertheless, we were able to obtain some individual RVs for this (much) cooler component (cf. Sect. 4.4).

## 3. Methodology

The orbital motion of a binary system causes a periodic fluctuation of the light path and its associated travel time with respect to the system's centre of mass. On the other hand, light from a source in motion undergoes a (Doppler) shift of its frequency. In the frequency domain (for a time base  $T \gg P_{\text{orb}}$ ), this phenomenon corresponds to a frequency modulation (FM) which can be detected as a frequency multiplet whose exact spacing is the orbital frequency (Shibahashi & Kurtz 2012). In the time domain (for  $T \ll P_{\text{orb}}$ ), this effect corresponds to a modulation of the phase (PM) with the orbital period, whose amplitude depends on the mass of the (unseen) companion and the observed frequency (Murphy et al. 2014). Hence, if one of the components is a pulsating star, the change in the light travel time introduces periodic phase shifts of each individual (pulsation) frequency. By converting the phase shift into a time delay, the frequency dependency is removed. Therefore, if the star is a multiperiodic pulsator, all the pulsation frequencies will experience the same time delay.

Murphy et al. (2014) described the principle of obtaining time delays from observed phase shifts of the pulsations and applied the PM method unto various cases of *Kepler* pulsating stars in (non-eclipsing) binary systems, while Murphy & Shibahashi (2015) provided an analytical method for solving the orbit, also in highly eccentric cases. This method is in essence similar to the search for variability in the (O-C)'s, the residuals in the times of specific phases in the light curve of periodically pulsating stars which are members of a binary system (e.g. Moffett et al. 1988; Fauvaud et al. 2010). Murphy et al. (2016) presented examples of orbital analyses combining radial velocities (RVs) with photometric time delays (TDs), and discussed some of the limitations and advantages. In this study, we developed and applied our own code for a simultaneous least-squares fitting of our updated RVs and the TDs based on the *Kepler* data. Both quantities are functions of the same orbital parameters: the time delay corresponds to the light travel time and the radial velocity is the time derivative of the position along the orbital path projected in the observer's direction. We consider the following equations as our model:

$$\text{TD}(t) = \frac{a \sin i}{c} \frac{1 - e^2}{1 + e \cos(\nu(t))} \sin(\nu(t) + \omega) \quad (1)$$

$$V(t) = 2\pi \frac{a \sin i}{P \sqrt{1 - e^2}} (\cos(\nu(t) + \omega) + e \cos \omega) + V_y, \quad (2)$$

where the true anomaly  $\nu$  is a function of  $t$ ,  $T_0$ ,  $P$  and  $e$ ,  $T_0$  is the time of periastron passage,  $P$  is the orbital period,  $a \sin i$  is the projected semi-major axis,  $e$  is the eccentricity,  $\omega$  is the

longitude of the periastron,  $V_\gamma$  is the systemic velocity and  $c$  is the speed of light. Equ. 1 is given by Irwin (1952) (see Pribulla et al. 2005). We removed a linear trend from the original TDs computed with Equ. 1 (Murphy et al. 2016) in order to convert the pulsation frequencies to their intrinsic values, i.e. unaffected by the variable light travel time of the pulsating component. This correction is necessary since the frequencies used for computing the TDs may be biased by the (uneven) orbital phase coverage of the *Kepler* data, thereby introducing a bias in the TDs themselves (as in the (O-C) curves).

In Paper I, we computed the time-dependent phases for up to 20 frequencies of highest  $S/N$  (generally the ones located in the  $p$ -mode regime) for all 49 targets of our sample. We thus uncovered nine objects for which correlated variations of comparable amplitude in the TDs were observed. In six systems, we could attribute the TD variations to orbital motion of a binary or multiple system. By analysing the RV and the TD data together, we are able to refine the orbital solutions and obtain stronger constraints on (some of) the orbital parameters and their derived parameters. Since the TDs are generally determined from the high(er) frequencies, they only provide information on the origin of the  $\delta$  Scuti-type pulsations associated to these frequencies. However, it is much harder to identify the origin of the low(er) frequencies ( $\gamma$  Doradus-type) due to their longer periods. In the next sections, we will analyse each of the four systems just described and highlight the gains that may be obtained from such modelling.

## 4. Orbital solutions from combined modelling

### 4.1. The triple system KIC 4480321

KIC 4480321 is a triple system (SB3) whose orbital periods are estimated to be 9.166 and  $\sim 2280$  d (Sect. 2.1). We computed the phase shifts and their associated TDs for frequencies of highest  $S/N$  and evidenced the presence of long-term variations which are coherent with the long-term RV variability (Paper I, fig. 24). We remark that the TDs were corrected by removing a linear trend from the original data (as everywhere). We then performed a simultaneous least-squares fitting of three updated component RVs and the mean TDs with their respective uncertainties. The best fit in the sense of  $\min \chi^2$  was obtained when we associated the TDs with the RVs of the fast spinning, more luminous A-type star (component C). Fig. 1 illustrates the quality of the fit showing the outer orbital solution together with both data types. The TDs and the RVs are overlaid with the AB-C orbital solution. Note that the TD curve mimics the RV curve but with an apparently larger eccentricity and a  $90^\circ$  shift in periastron longitude (Irwin 1952). The revised orbital parameters of the coupled solutions are listed in Table 2. Compared to Paper I, we see that the orbital solution of the A-B system is robust and well-determined while the outer orbital solution changed profoundly. The orbital period is longer ( $P_{\text{orb}} \sim 2380$  d) and better determined than before (see also Murphy et al. 2018), while the eccentricity and the semi-axis major increased substantially. Thus, the minimum component mass  $M_C \sin^3 i_{\text{out}}$  increased to  $1.60 \pm 0.05 M_\odot$ . The strongest improvement concerns the accuracy and robustness of the outer orbital solution. This is due to two things: (a) by combining both data types, we dispose of a time base longer than eight years and (b) the TDs concern the fast-rotating component C for which the RVs show the largest scatter. We therefore were able

Table 2: Values and standard deviations of the constrained orbital parameters for KIC 4480321. Note that from hereon, for all similar tables,  $T_0$  is expressed in Hel. JD - 2,400,000. and  $rms$  indicates the standard deviation of the squared residuals.

Orbital solution A-B		
Orbital parameter	Value	Std. dev.
$P$ (d)	9.16585	0.00015
$T_0$ (Hel. JD)	58503.065	0.015
$e$	0.07894	0.00097
$\omega$ ( $^\circ$ )	351.1	0.6
$V_\gamma$ (km s $^{-1}$ )	(var.)	
$a_A \sin i$ (au)	0.04779	0.00006
$a_B \sin i$ (au)	0.04876	0.00006
$K_A$ (km s $^{-1}$ )	56.90	0.07
$K_B$ (km s $^{-1}$ )	58.05	0.07
$M_A \sin^3 i$ ( $M_\odot$ )	0.7216	0.0019
$M_B \sin^3 i$ ( $M_\odot$ )	0.7073	0.0019
$q_{\text{in}}$	0.980	0.002
$rms_A$ (km s $^{-1}$ )	1.486	
$rms_B$ (km s $^{-1}$ )	0.455	
Orbital solution AB-C		
Orbital parameter	Value	Std. dev.
$P$ (d)	2381.	5.9
$T_0$ (Hel. JD)	59082.	13.
$e$	0.140	0.006
$\omega$ ( $^\circ$ )	197.9	1.8
$V_\gamma$ (km s $^{-1}$ )	-19.97	0.04
$a_{AB} \sin i_{\text{out}}$ (au)	2.232	0.013
$a_C \sin i_{\text{out}}$ (au)	3.293	0.076
$a_{\text{TDc}}/c \sin i_{\text{out}}$ (d)	0.0190	0.0004
$K_{AB}$ (km s $^{-1}$ )	10.30	0.07
$K_C$ (km s $^{-1}$ )	15.20	0.35
$M_{AB} \sin^3 i_{\text{out}}$ ( $M_\odot$ )	2.36	0.12
$M_C \sin^3 i_{\text{out}}$ ( $M_\odot$ )	1.60	0.05
$q_{\text{out}}$	0.678	0.016
$rms_C$ (km s $^{-1}$ )	4.689	
$rms_{\text{TD}}$ (d)	0.0012	

to determine a (much) improved mass ratio for the outer system and to provide (more) reliable values of the three minimum component masses. From the minimum total mass of the A-B system derived for each orbit, we get  $\sin i = 0.846 (\pm 0.028)$   $\sin i_{\text{out}}$ , from which we obtain the condition  $i < 58^\circ$  for the inner orbit. We may furthermore attribute the  $\delta$  Scuti pulsations to the more massive component C (the frequencies showing phase shifts are all located in the  $p$ -mode region). In summary, KIC 4480321 is a hierarchical triple system with  $q_{\text{in}} = M_B/M_A = 0.98$  and  $q_{\text{out}} = M_C/M_{AB} = 0.68$ .

### 4.2. The triple system KIC 5219533

KIC 5219533 was classified as triple (SB3) with an inner pair of Am-like stars and with orbital periods of 31.919 and  $\sim 1615$  d (Sect. 2.2). For this system, we also detected long-term variations of the TDs in agreement with the long-term change observed in the RVs (Paper I, fig. 24). We performed a simultaneous least-squares fitting of the updated component RVs and the mean TDs with their respective uncertainties, and obtained the best fit in the sense of  $\min \chi^2$  with the TDs assigned to

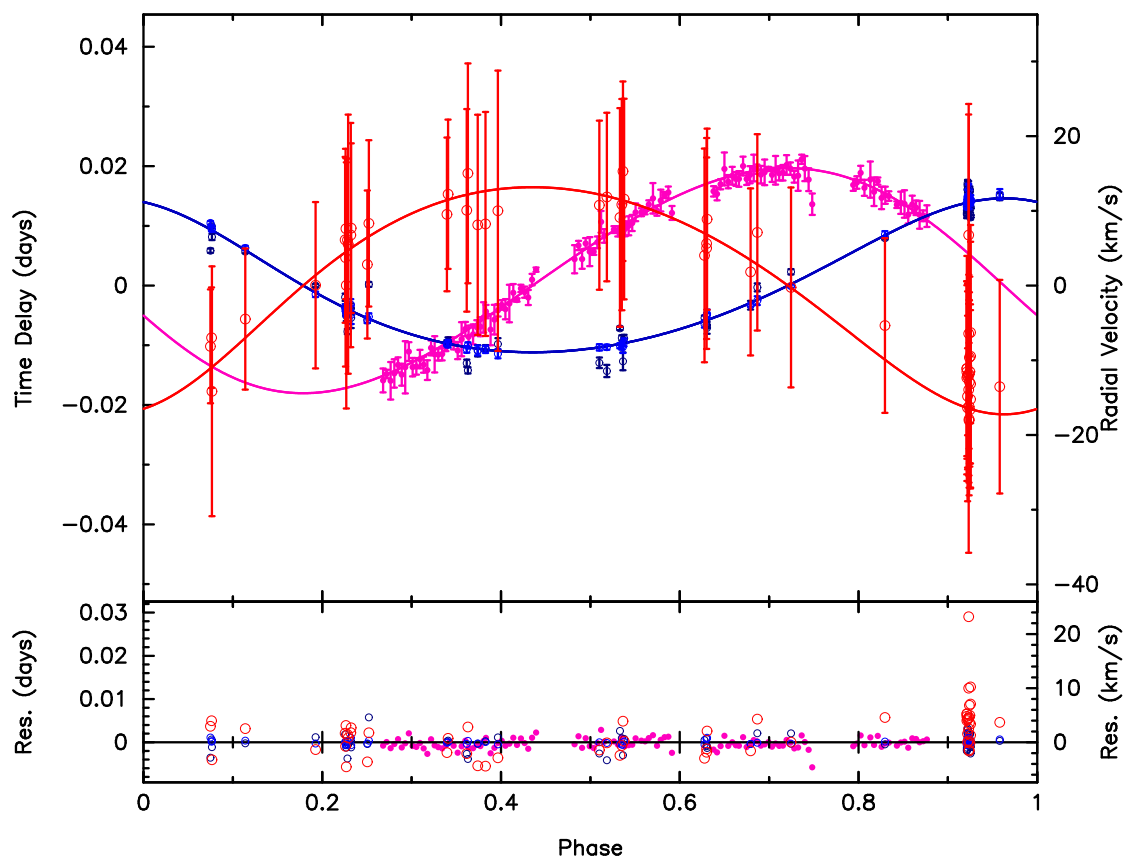


Fig. 1: Data and outer orbital solution for KIC 4480321. The TDs and RVs (resp. filled pink and unfilled red symbols for component C; blue symbols for the centre of mass of components A and B) are overlaid with the AB-C orbital solution (solid lines). The residuals are shown in the bottom panel.

the outer companion (component C). Since this component is heavily diluted in the composite spectrum, its RVs are not well-determined. However, a modelling of the combined data allows to derive full orbital solutions. The new parameters of the inner and outer orbital solutions are presented in Table 3. Fig. 2 illustrates the quality of the fit as well as both solutions. The mean residuals of the component RVs stay below  $1 \text{ km s}^{-1}$ . The largest residuals are found near the nodal passage (both components have similar RVs). The orbital solution of the A-B pair is in good agreement with the one proposed by Catanzaro et al. (2019a), though our semi-major axes are slightly larger (and our component masses a bit smaller) than theirs. Indeed, their Figs. 3 and 4 show that several HERMES RVs (open symbols) lie a bit off from their final solution. The overall gain in accuracy for most parameters of the inner orbital solution is a factor of 5, while the orbital period is 10 times more accurate. We cannot compare the mean RV residuals since these were not displayed. In Fig. 2 (right), the TDs and the RVs are plotted together with the revised AB-C orbital solution. We thus determined the semi-axis major of component C and the minimum mass of the A-B pair for the first time. The gain is largest for the outer orbit since the accuracy on the parameters improved with a mean factor of 10 while the orbital period is about 30 times more accurate compared to Catanzaro et al. (2019a). In particular, we obtained the minimum component masses  $M_A \sin^3 i = 1.336 \pm 0.005$ ,  $M_B \sin^3 i = 1.293 \pm 0.004$  and  $M_C \sin^3 i_{\text{out}} = 1.47 \pm 0.02 M_\odot$ . From the minimum total mass of the A-B system derived for each orbit leading to the condition  $\sin i_{\text{out}} = 0.996 (\pm 0.009) \sin i$ , we infer that both orbits are very

close to coplanarity. In summary, KIC 5219533 is a hierarchical, probably coplanar system with  $q_{\text{in}} = 0.97$  and  $q_{\text{out}} = 0.57$ . We furthermore established that the  $\delta$  Scuti pulsations are linked to the more massive, faster rotating star in the system.

#### 4.3. KIC 8975515

This star was recognized as SB2 from our multi-epoch study, and also shows long-term variations of the TDs coherent with the variations found in the RVs (Paper I, fig. 24). The system consists of late A-type stars with one fast spinning (component A) and one (apparently) slowly spinning star (component B). In Paper I, we derived an orbital solution of type SB1 based on the RVs of component B only ( $P_{\text{orb}} \sim 1600 \text{ d}$ ). We first derived a pure RV-based orbital solution (using the RVs of both components). Unfortunately, the extreme uncertainties on the RVs of the fast spinning component did not allow to constrain its RV amplitude. This is obvious in Fig. 3 (left) which illustrates the best-fit orbital solution with a period of 1581 d. Subsequently, we performed two simultaneous (RV+TD) analyses, by associating the TDs with each set of RVs in turn, and found an optimum fit when the TDs were assigned to component A.

We determined an orbital period of  $1603.4 \pm 9.3 \text{ d}$ . The new orbital parameters and their derived fundamental properties are listed in Table 4. The residuals show the very good agreement between both data types, with small mean residuals for the TDs and RVs of component B (the slower rotator), and a large (non-zero) mean residual for component A (the faster rotator).

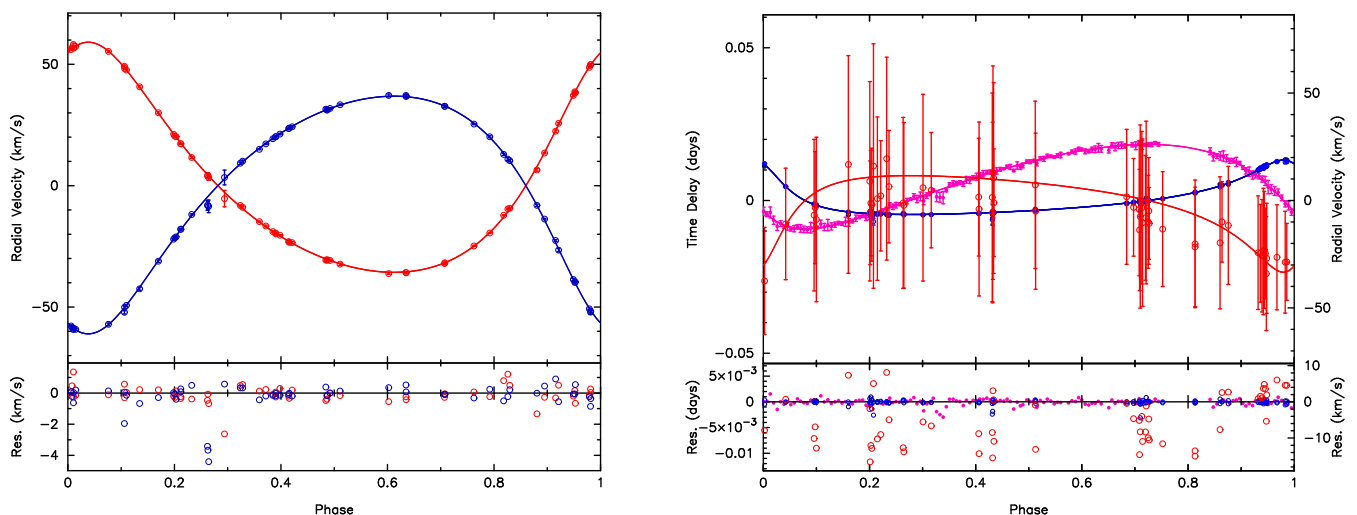


Fig. 2: Data and orbital solutions for KIC 5219533. *Left*: Inner orbit based on the HERMES RVs. The RVs (red symbols for component A; blue symbols for component B) are overlaid with the A-B orbital solution (solid lines). *Right*: Outer orbit based on the HERMES RVs and the TDs from the *Kepler* photometry. The TDs and RVs (resp. filled pink and unfilled ed symbols for component C; blue symbols for the centre of mass of components A and B) are overlaid with the AB-C orbital solution (solid lines). The residuals are shown in the bottom panels.

Table 3: Values and standard deviations of the constrained orbital parameters for KIC 5219533.

Orbital solution A-B		
Orbital parameter	Value	Std. dev.
$P$ (d)	31.91763	0.00022
$T_0$ (Hel. JD)	57467.41	0.02
$e$	0.271	0.001
$\omega$ ( $^\circ$ )	335.3	0.2
$V_\gamma$ (km s $^{-1}$ )	(var.)	
$a_A \sin i$ (au)	0.13369	0.00019
$a_B \sin i$ (au)	0.13810	0.00023
$K_A$ (km s $^{-1}$ )	47.33	0.07
$K_B$ (km s $^{-1}$ )	48.90	0.08
$M_A \sin^3 i$ ( $M_\odot$ )	1.336	0.005
$M_B \sin^3 i$ ( $M_\odot$ )	1.293	0.004
$q_{in}$	0.968	0.002
$rms_A$ (km s $^{-1}$ )	0.550	
$rms_B$ (km s $^{-1}$ )	0.833	
Orbital solution AB-C		
Orbital parameter	Value	Std. dev.
$P$ (d)	1603.5	1.7
$T_0$ (Hel. JD)	55212.9	3.2
$e$	0.564	0.004
$\omega$ ( $^\circ$ )	210.6	0.5
$V_\gamma$ (km s $^{-1}$ )	10.70	0.04
$a_{AB} \sin i_{out}$ (au)	1.542	0.008
$a_C \sin i_{out}$ (au)	2.74	0.03
$a_{TDc}/c \sin i_{out}$ (d)	0.0158	0.0002
$K_{AB}$ (km s $^{-1}$ )	12.67	0.08
$K_C$ (km s $^{-1}$ )	22.49	0.27
$M_{AB} \sin^3 i_{out}$ ( $M_\odot$ )	2.60	0.07
$M_C \sin^3 i_{out}$ ( $M_\odot$ )	1.47	0.02
$q_{out}$	0.565	0.006
$rms_C$ (km s $^{-1}$ )	8.294	
$rms_{TD}$ (d)	0.0006	

Table 4: Values and standard deviations of the constrained orbital parameters for KIC 8975515.

Orbital solution A-B		
Orbital parameter	Value	Std. dev.
$P$ (d)	1603.4	9.3
$T_0$ (Hel. JD)	58690.	19.
$e$	0.408	0.015
$\omega$ ( $^\circ$ )	172.5	2.6
$V_\gamma$ (km s $^{-1}$ )	-20.63	0.14
$a_A \sin i$ (au)	0.3988	0.0053
$a_B \sin i$ (au)	0.483	0.028
$a_{TD_A}/c \sin i$ (d)	0.00230	0.00003
$K_A$ (km s $^{-1}$ )	2.96	0.05
$K_B$ (km s $^{-1}$ )	3.59	0.21
$M_A \sin^3 i$ ( $M_\odot$ )	0.0195	0.0024
$M_B \sin^3 i$ ( $M_\odot$ )	0.0161	0.0011
$q$	0.83	0.05
$rms_A$ (km s $^{-1}$ )	2.597	
$rms_B$ (km s $^{-1}$ )	0.237	
$rms_{TD}$ (days)	0.00013	

The orbital solution is illustrated in Fig. 3 (right). In this case, the mass ratio ( $q = 0.83 \pm 0.05$ ) is well-determined thanks to the high accuracy of the TDs (whereas the corresponding component RVs show a very large scatter). The present method allowed us to derive information which was otherwise impossible to obtain with a pure RV-based solution. Another conclusion is that the faster rotating component exhibits the  $\delta$  Scuti pulsations. This may also explain why the RV residuals of component A are found to be systematically off from the final solution. From the parameters displayed in Table 4, we obtain the minimum masses,  $M_A \sin^3 i = 0.0195 \pm 0.0024$  and  $M_B \sin^3 i = 0.0161 \pm 0.0011 M_\odot$ . Assuming that either one of the components has a typical mass of  $\sim 2 M_\odot$ , we expect that the system is seen under a low inclination angle ( $i \sim 12^\circ$ ).

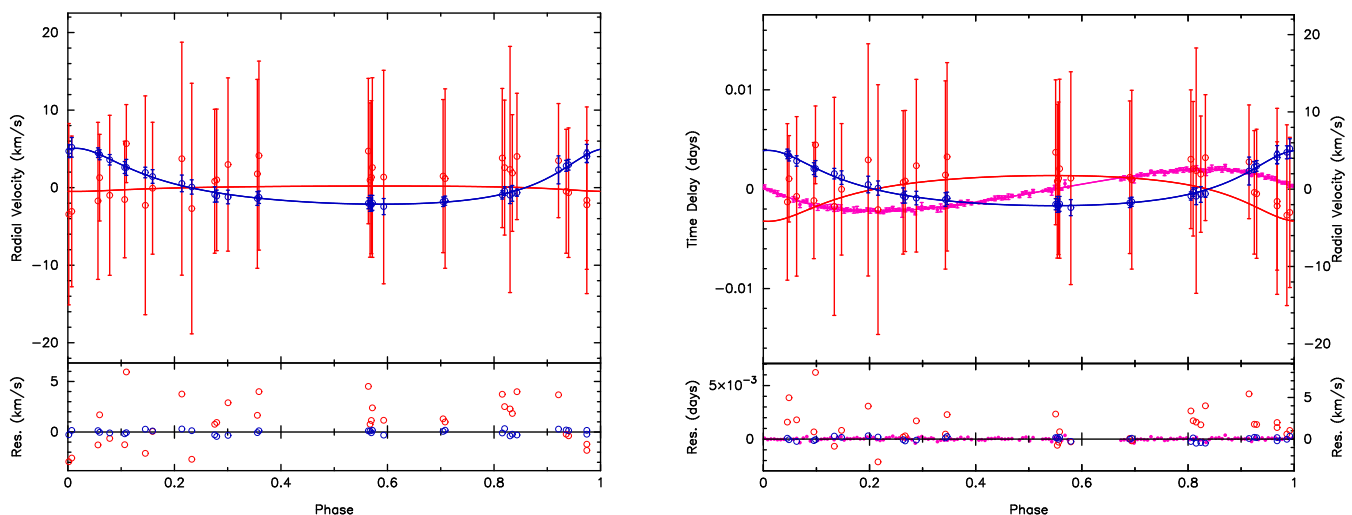


Fig. 3: Data and orbital solution for KIC 8975515. *Left*: Orbit (nr 1) based on the HERMES RVs. The RVs (red symbols for component A; blue symbols for component B) are overlaid with a preliminary orbital solution of type SB2, however without much constraint on the amplitude  $K_A$ . *Right*: Orbit (nr 2) based on the HERMES RVs and the TDs from the *Kepler* photometry. The TDs and RVs (resp. filled pink and unfilled red symbols for component A; blue symbols for component B) are overlaid with the A-B orbital solution (solid lines). The residuals are shown in the bottom panels.

#### 4.4. KIC 9775454

KIC 9775454 was classified as a long-period SB1 (Sect. 2.4). It was shown to display long-term variations of the TDs in agreement with the orbital variations of the RVs (this concerns also the dominant frequency located at  $4.161 \text{ d}^{-1}$ , cf. Paper I). Murphy et al. (2018) used the HERMES RVs of the broad-lined primary (component A) and derived an orbital solution with a period of  $\sim 1700$  days from their combined (RV+TD) analysis. Being much fainter, component B was not directly detected in the high-resolution spectra. Nevertheless, we managed to find an indication of a cool companion by computing CCFs of the residual spectra (after proper subtraction of an adequate synthetic spectrum to remove the contribution of the primary) using a mask of spectral type K0. The “residual” CCFs were computed for the spectral range  $[5100 - 5700] \text{ \AA}$ , and revealed a shallow peak that reflects the contribution of the companion and displays Doppler shifts (Fig. 5). In this way, we were able to extract additional RV data which behave in anti-phase with those of component A (Fig. 4). We roughly estimated their uncertainties from the widths of the associated spectral lines. Thus, we can classify KIC 9775454 as an SB2. We next performed a simultaneous (RV+TD) analysis, by fitting the component RVs together with the TDs assigned to the broad-lined primary (component A). The new orbital solution is illustrated by Fig. 4. The RV residuals of component A and the TD residuals are within expectation while the RV residuals of component B are systematically large. This can be explained by the noisy “residual” CCFs associated to the difficulty of identifying the lines of the cool component in the spectra. The orbital parameters and derived fundamental properties are listed in Table 5. These parameters agree very well with the values proposed by Murphy et al. (2018). By treating this system as an SB2 and using the TDs, we determined for the first time a reasonable value of the mass ratio ( $q = 0.42 \pm 0.02$ ). In this special case where the TDs are linked with both the low- and the high-frequency regions, the more massive primary component is very likely the hybrid pulsator.

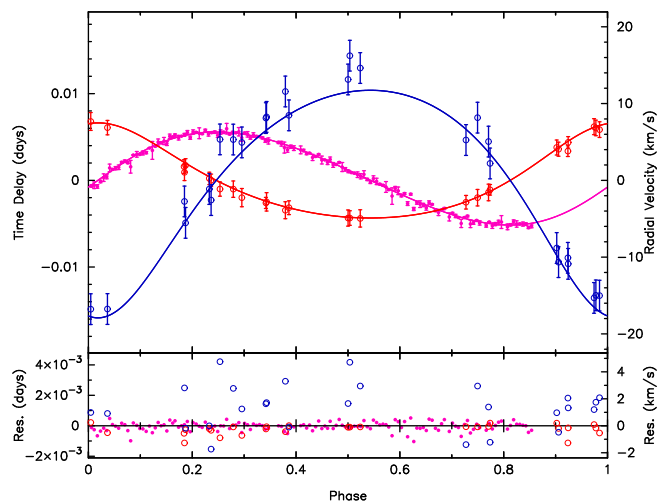


Fig. 4: Data and orbital solution for KIC 9775454. The TDs (filled pink symbols) and the RVs (unfilled red symbols for component A; blue symbols for component B) are overlaid with the A-B orbital solution (solid lines). The residuals are shown in the bottom panel.

## 5. Search for regular frequency patterns

In this section, we investigate the distributions of the frequency differences (aka spacings) that occur in the high-frequency regime of the Fourier transforms of each system. The aim is to identify the (most) frequently occurring frequency spacings for each object, and to verify whether some of these spacings might be related to the orbital or the rotational periods. In the case of an orbital or a rotational origin of the low frequencies (e.g. due to modulations in the light curve caused by the tidal deformations or by the presence of spots or other surface inhomogeneities e.g. MOBSTER (Sikora et al. 2019) or caused by the mechanism of tidal excitation e.g. KIC 4142768 (Guo et al. 2019)), we may expect to detect a significant number of harmonics of the corresponding main frequencies. In the case of

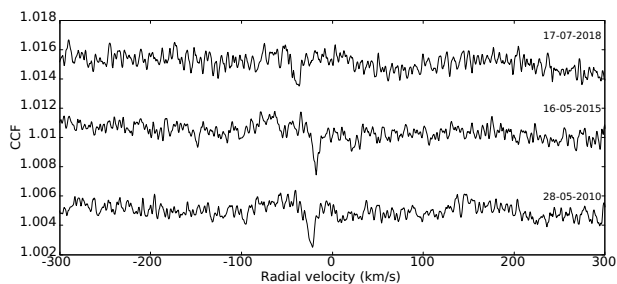


Fig. 5: CCFs of the residual spectra of KIC 9775454 computed with a mask of type K0 for three different dates.

Table 5: Values and standard deviations of the constrained parameters of the orbital solution for KIC 9775454.

Orbital solution A-B		
Orbital parameter	Value	Std. dev.
$P$ (d)	1706.8	6.4
$T_0$ (Hel. JD)	56655.	10.
$e$	0.212	0.008
$\omega$ ( $^\circ$ )	349.6	1.9
$V_\gamma$ ( $\text{km s}^{-1}$ )	-22.15	0.16
$a_A \sin i$ (au)	0.949	0.017
$a_B \sin i$ (au)	2.27	0.09
$a_{TD_A} / c \sin i$ (d)	0.00548	0.00010
$K_A$ ( $\text{km s}^{-1}$ )	6.19	0.12
$K_B$ ( $\text{km s}^{-1}$ )	14.82	0.62
$M_A \sin^3 i$ ( $M_\odot$ )	1.08	0.11
$M_B \sin^3 i$ ( $M_\odot$ )	0.45	0.03
$q$	0.42	0.02
$rms_A$ ( $\text{km s}^{-1}$ )	0.471	
$rms_B$ ( $\text{km s}^{-1}$ )	2.150	
$rms_{TD}$ (d)	0.00028	

a tidal or rotational splitting of the high frequencies associated to the rapid pulsations (e.g. of tidal splitting of  $p$ -modes in KIC 6048106 and U Gru, respectively, Samadi Ghadim et al. 2018; Bowman et al. 2019), we may expect to find regular (also non-harmonic) frequency patterns whose spacing values will point at those frequencies.

We used the detrending algorithm of Lightkurve v1.9 to detrend the *Kepler* light curves of the previously discussed systems (Barentsen & Lightkurve Collaboration 2020), and computed the periodograms with the Lomb-Scargle technique (Fig. 6). For each system, we analysed the frequency interval of the periodogram where most of the power is located. For KIC 4480321, this corresponds to the  $[12.5, 24.7]$   $\text{d}^{-1}$  interval; for KIC 5219533, this is the  $[6, 22.5]$   $\text{d}^{-1}$  interval; for KIC 8975515, the  $[12.5, 17.5]$   $\text{d}^{-1}$  interval, and for KIC 9775454, the  $[5.7, 22.5]$   $\text{d}^{-1}$  interval. We then computed the spacings between all possible pairs of significant frequencies while considering the limiting frequency resolution of the *Kepler* long-cadence data sets, and counted the number of individual occurrences (as in Samadi Ghadim et al. 2018).

We next discuss the density distributions of the frequency spacings derived from the *Kepler*-based periodograms for the four systems with the improved orbits. The density plots of the frequency spacings were produced from the counts adopting a bin size of  $0.05 \text{ d}^{-1}$  in each case. In Fig. 7, we show the density

plots of the spacings for KIC 4480321, 5219533, 8975515 and KIC 9775454 in the restricted frequency range  $[0 - 4] \text{ d}^{-1}$ , i.e. the interval where the highest occurrences can be found. A general observation is that the distributions of the frequency spacings in the high-frequency regime of the four systems show large differences between them. Also, a high(er) peak in the distributions (or a secondary maximum) of individual spacings is generally located in the first bin. This is due to the fact that this bin also contains the smallest possible spacing which corresponds to the frequency resolution of  $0.00068 \text{ d}^{-1}$  in the *Kepler* long-cadence data.

From Fig. 7, we derived the following findings:

- Both KIC 4480321 and KIC 5219533 present a dense and continuous distribution of frequency spacings with several (almost) equal local maxima. There is power everywhere, also in the first bin. The close binaries of these triple systems have orbital frequencies of respectively  $0.11 \text{ d}^{-1}$  and  $0.03 \text{ d}^{-1}$ , which means that in the case of KIC 4480321, the bin size is small enough to draw a firm conclusion with respect to tidal splitting. In the case of the remaining binary systems, the orbital periods are of order of several years and too large to be resolved in the periodograms. In the case of KIC 4480321, the highest occurrences occur at the spacings of 0.35, 1.63 (highest), and  $3.33 \text{ d}^{-1}$ . The latter spacing shows a harmonic relation with  $1.63 \text{ d}^{-1}$  (ratio of almost 2). This interdependence between two frequent spacings could be very well explained by rotation. Also, Li et al. (2020b) derived  $0.0070 \pm 0.0007 \text{ d}^{-1}$  for the near-core rotation rate from a modelling of the slope-period relation based on the regular period spacings in the  $g$ -mode region. Such a fast rotation rate stands in sharp contrast with the the abovelisted most frequent spacings if we consider them as potential surface rotation rates for component C (the fast-spinning component). On the other hand, we find no peak occurring near or at the orbital frequency value of  $0.11 \text{ d}^{-1}$ . We conclude that the orbital frequency of the inner binary system does not affect the pulsation frequencies in the  $p$ -mode region. This is perfectly consistent with the conclusion that component C is the  $\delta$  Scuti pulsator.

- In the case of KIC 5219533, the most frequent spacings occur at the frequencies of 0.55, 0.94 (highest) and  $2.32 \text{ d}^{-1}$ , (or the equally frequent spacings at 2.98 and  $3.59 \text{ d}^{-1}$ ). The frequent spacings of 0.55 and  $0.94 \text{ d}^{-1}$  could indicate the rotation period of component C (the fast-spinning component). We note that Li et al. (2020b) derived  $0.59 \pm 0.01 \text{ d}^{-1}$  for the near-core rotation rate based on their modelling. This seems to match the smallest value of the frequent spacings (i.e.  $0.55 \text{ d}^{-1}$ ). The orbital period of the inner binary is  $\sim 32$  d, which implies that the corresponding frequency (at  $0.03 \text{ d}^{-1}$ ) would be located in the first bin. Thus, we cannot infer from this plot whether or not this frequency is affecting the higher pulsation frequencies. However, the most frequent individual spacing occurs at  $0.0012 \text{ d}^{-1}$ , which is far away from the orbital frequency of the inner pair.

- KIC 8975515 presents an irregular distribution of unequal peaks, though of much lower density. The two highest occurrences (except for the first bin) occur at 2.10 (highest) and  $3.76 \text{ d}^{-1}$ , closely followed by  $1.06 \text{ d}^{-1}$ . Again, the ratio of  $\sim 2$  between two of the three most frequent spacings indicates that rotation might be the relevant mechanism to explain the presence of a frequent spacing and its harmonic. However, the frequency spacing of  $1.66 \text{ d}^{-1}$ , which probably corresponds to the rotation frequency of the fast-rotating hybrid pulsating component in the system (Samadi-Ghadim et al. 2020), is the highest occurrence among the individual spacings. Li et al. (2020b) derived  $1.85 \pm 0.01 \text{ d}^{-1}$  for the near-core rotation rate.

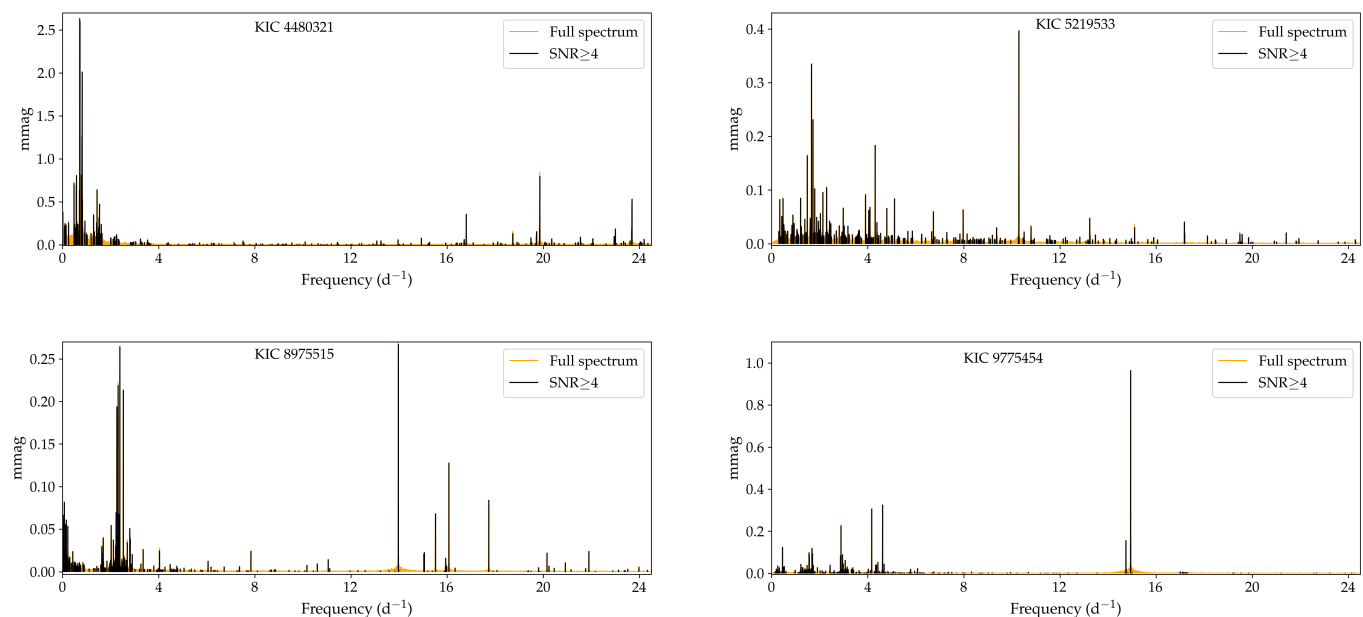


Fig. 6: Lomb-Scargle periodograms derived from the *Kepler* data for the systems KIC 4480321 (top left), 5219533 (top right), 8975515 (bottom left) and KIC 9775454 (bottom right). The frequencies plotted in orange illustrate the full spectrum across the range  $[0 - 24.5] \text{ d}^{-1}$ , while the frequencies overplotted in black have a signal-to-noise ratio higher than 4.

If this rate corresponds to the faster rotating component, the core versus surface rotation ratio would equal  $1.11 \pm 0.01$ , as expected from the general trend found by Li et al. (2020b). The frequent spacing of  $1.06 \text{ d}^{-1}$  might correspond to the more slowly-rotating  $\delta$  Scuti component, although Samadi-Ghadim et al. (2020) proposed a rotation rate of  $0.42 \text{ d}^{-1}$ . In this case, the orbital frequency is unresolved.

- KIC 9775454 shows a remarkably sparse distribution in frequency spacing. The two highest peaks (except for the first bin) occur at the spacings of  $0.13$  and  $2.18 \text{ d}^{-1}$  (highest). The latter and most frequent spacing is accompanied by a few nearby, almost equally frequent spacings located at  $2.07$ ,  $2.26$  and  $2.35 \text{ d}^{-1}$ . This suggests that one of these frequency spacings is the rotational frequency of the hybrid pulsator (comp A) (in the case of  $\sim 2 \text{ d}^{-1}$ , it is probably variable). If we consider the fact that the primary component has  $v \sin i = 65 \text{ km s}^{-1}$ , adopting a default radius of  $1.8 R_{\odot}$  corresponding to its  $T_{\text{eff}}$  (Gorda & Svechnikov 1998) and the frequency of  $2.18 \text{ d}^{-1}$  as the rotational frequency, implies  $v_{\text{eq}} = 199 \text{ km s}^{-1}$  and a surface inclination angle of  $\sim 19^{\circ}$  as possible values. The alternative choice (with  $0.13 \text{ d}^{-1}$ ) would give an impossible value of  $12 \text{ km s}^{-1}$  for  $v_{\text{eq}}$ . The orbital frequency is unresolved here as well.

## 6. Summary and conclusions

In the previous sections, we improved the orbital solutions for four spectroscopic systems from our sample of 49 A/F-type *Kepler* hybrid stars. We improved the orbital solutions for the following spectroscopic systems: KIC 4480321, 5219533, 8975515 and KIC 9775454 by considering the TDs as well as the RVs and performing a simultaneous modelling of both data types. This method allowed us to refine the parameters of all the long-period systems, in particular the outer orbits of the triple systems KIC 4480321 and KIC 5219533. We derived full-fledged SB2 orbital solutions for the long-period

binary systems KIC 8975515 and KIC 9775454 and obtained reliable mass ratios for the first time. Furthermore, the applied methodology enabled us to identify the component with the faster  $\delta$  Sct-type pulsations, since the TDs are generally linked with the higher frequencies.

For KIC 4480321, we concluded that the faster rotating and more massive outer component (comp C) exhibits the short-period  $\delta$  Scuti pulsations. Component C was shown to have a minimum mass of  $1.60 \pm 0.05 M_{\odot}$ , which can be used as a constraint for asteroseismic modelling. For KIC 5219533, we significantly improved the accuracy of the orbital solutions described by Catanzaro et al. (2019a). We also showed that both orbits are very probably coplanar and that the  $\delta$  Scuti pulsator is the faster spinning and more massive outer component (comp C). For KIC 8975515, we derived an accurate mass ratio ( $q = 0.83 \pm 0.05$ ) and established that the faster rotating component (comp A) exhibits  $\delta$  Scuti-type pulsations (this concerns the hybrid pulsator). Furthermore, the binary is probably viewed under a low inclination angle ( $\approx 12^{\circ}$ ). The latter is also useful information in an asteroseismic context. For KIC 9775454, we determined a precise mass ratio for the first time ( $q = 0.42 \pm 0.02$ ). We concluded that the more massive component of the system (comp A) is the hybrid pulsating star.

From our study of the normalized distributions of the frequency spacings in the high-frequency regime of the Fourier transforms, we find no firm evidence for the occurrence of tidal splitting among the frequent spacings of the triple systems with close (inner) companions. In the case of the long-period orbits (all systems), it is impossible to resolve the frequency multiplets based on the *Kepler* data only. On the other hand, due to the presence of some harmonic frequencies among the most frequent spacings, we propose the mechanism of rotational splitting for KIC 4480321 (with a plausible surface rotation rate of  $1.63 \text{ d}^{-1}$ ), KIC 5219533 (with a possible surface rotation

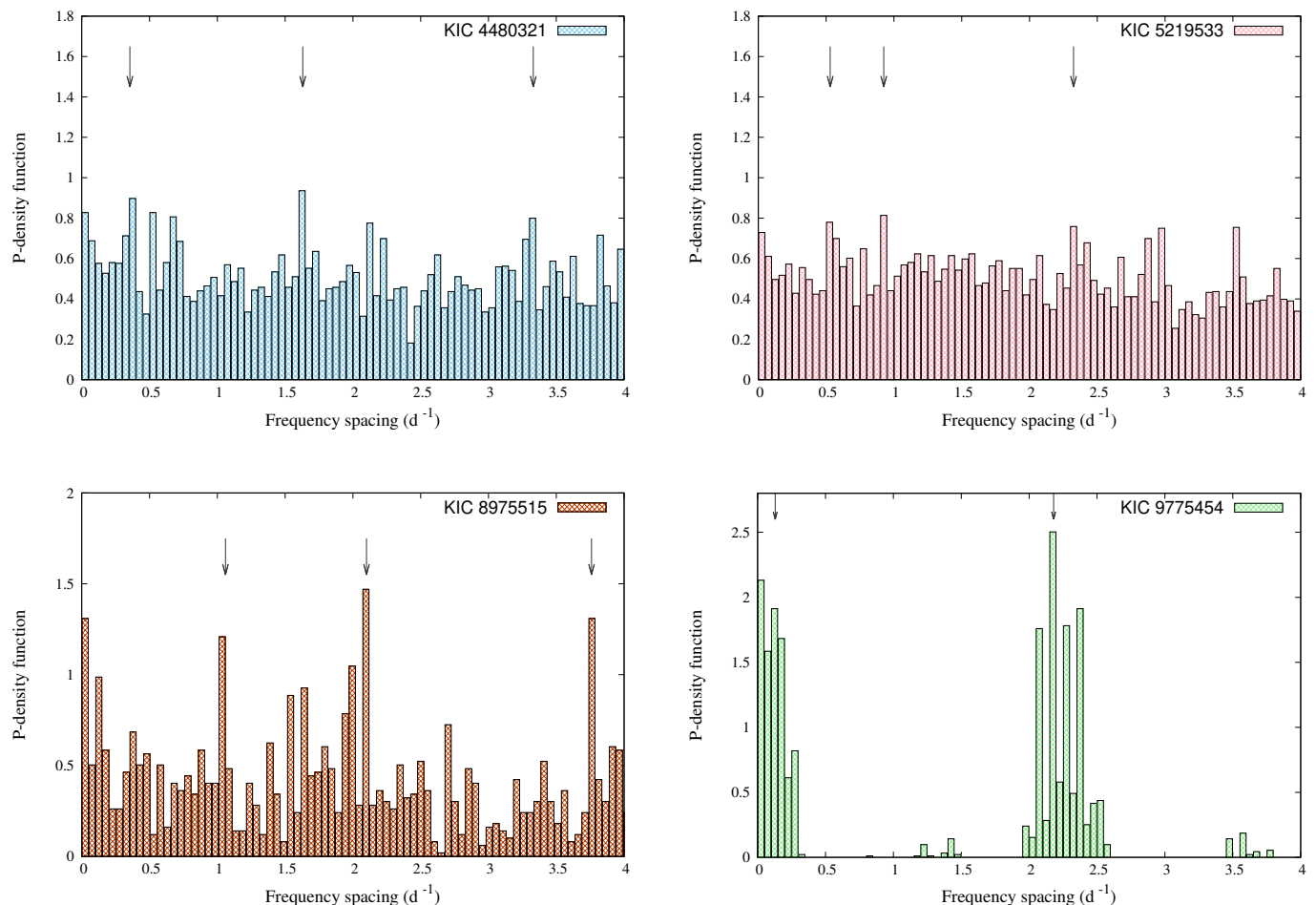


Fig. 7: Normalized density functions of the frequency spacings across the range  $[0 - 4] \text{ d}^{-1}$  derived from the *Kepler*-based periodograms for the systems KIC 4480321 (top left), 5219533 (top right), 8975515 (bottom left) and KIC 9775454 (bottom right). The highest occurrences are marked by grey arrows.

rate of  $0.55 \text{ d}^{-1}$ ) and KIC 8975515 (with a possible surface rotation rate of  $1.06 \text{ d}^{-1}$  for the secondary component, whereas the primary rotates at the rate of  $1.66 \text{ d}^{-1}$ ). In the particular case of KIC 9775454, we propose a surface rotation rate of the order of  $2 \text{ d}^{-1}$ , which appears as a bunch of closely spaced frequent spacings in the distribution and indicates a possibly variable nature. Detailed analyses of the pulsations in the low-frequency regime of the Fourier transforms of these systems, including pattern recognition and period spacings of the gravity (and sometimes Rossby) modes for the (rapidly rotating) genuine hybrid pulsators, can provide the near-core rotation rates and a confirmation of the proposed surface rotation rates (e.g., Van Reeth et al. 2016; Li et al. 2020b,a).

## Acknowledgements

The authors wish to thank the *Kepler* team for providing the high-quality data collected with the *Kepler* satellite mission. They furthermore thank the HERMES Consortium for enabling the production of the high-resolution ground-based spectra, and D. Bowman et al. for authorizing the use of the additional spectra of KIC 5219533. ÁS and ZsB acknowledge financial support of the Lendület Program LP2018-7/2019 of the Hungarian

Academy of Sciences. MS acknowledges the OV PPP Postdoc-MUNI grant with nr. CZ.02.2.69/0.0/0.0/16\_027/0008360 and the MSMT Inter Transfer program LTT20015. ZsB acknowledges the support provided by the National Research, Development and Innovation Fund of Hungary, financed under the PD<sub>17</sub> funding scheme (project PD-123910) and by the János Bolyai Research Scholarship of the Hungarian Academy of Sciences. HL acknowledges support from the grant DFG with nr. LE1102/3-1. ASG acknowledges financial support received from the ALMA-CONICYT grant with nr. 31170029. We thank the referee, Prof. H. Shibahashi, for detailed comments and constructive criticism. We are also grateful for support received from the Belgo-Indian Network for Astronomy & Astrophysics (BINA-1 and BINA-2).

## References

- Balona, L. A., Daszyńska-Daszkiewicz, J., & Pamyatnykh, A. A. 2015, *MNRAS*, 452, 3073
- Barentsen, G. & Lightcurve Collaboration. 2020, in American Astronomical Society Meeting Abstracts, American Astronomical Society Meeting Abstracts, 409.04
- Bowman, D. M. 2017, *Amplitude Modulation of Pulsation Modes in Delta Scuti Stars* (Springer International Publishing)
- Bowman, D. M., Johnston, C., Tkachenko, A., et al. 2019, *ApJ*, 883, L26

- Castelli, F. & Kurucz, R. L. 2003, in IAU Symposium, Vol. 210, Modelling of Stellar Atmospheres, ed. N. Piskunov, W. W. Weiss, & D. F. Gray, A20
- Catanzaro, G., Gangi, M., Giarrusso, M., Munari, M., & Leone, F. 2019a, MNRAS, 487, 919
- Catanzaro, G., Gangi, M., Giarrusso, M., Munari, M., & Leone, F. 2019b, MNRAS, 488, 480
- Fauvaud, S., Sareyan, J. P., Ribas, I., et al. 2010, A&A, 515, A39
- Gaia Collaboration. 2018, VizieR Online Data Catalog, I/345
- Gorda, S. Y. & Svechnikov, M. A. 1998, Astronomy Reports, 42, 793
- Grigahcène, A., Antoci, V., Balona, L., et al. 2010, ApJ, 713, L192
- Guo, Z., Fuller, J., Shporer, A., et al. 2019, ApJ, 885, 46
- Hubeny, I. & Lanz, T. 1995, ApJ, 439, 875
- Irwin, J. B. 1952, ApJ, 116, 211
- Lampens, P., Frémat, Y., Vermeylen, L., et al. 2018, A&A, 610, A17
- Li, G., Bedding, T. R., Murphy, S. J., et al. 2019, MNRAS, 482, 1757
- Li, G., Guo, Z., Fuller, J., et al. 2020a, MNRAS, 497, 4363
- Li, G., Van Reeth, T., Bedding, T. R., et al. 2020b, MNRAS, 491, 3586
- Moffett, T. J., Barnes, Thomas G., I., Fekel, Francis C., J., Jefferys, W. H., & Achtermann, J. M. 1988, AJ, 95, 1534
- Murphy, S. J., Bedding, T. R., Shibahashi, H., Kurtz, D. W., & Kjeldsen, H. 2014, MNRAS, 441, 2515
- Murphy, S. J., Moe, M., Kurtz, D. W., et al. 2018, MNRAS, 474, 4322
- Murphy, S. J. & Shibahashi, H. 2015, MNRAS, 450, 4475
- Murphy, S. J., Shibahashi, H., & Bedding, T. R. 2016, MNRAS, 461, 4215
- Nielsen, M. B., Gizon, L., Schunker, H., & Karoff, C. 2013, A&A, 557, L10
- Pribulla, T., Chochol, D., Tremko, J., & Kreiner, J. M. 2005, in Astronomical Society of the Pacific Conference Series, Vol. 335, The Light-Time Effect in Astrophysics: Causes and cures of the O-C diagram, ed. C. Sterken, 103
- Raskin, G., van Winckel, H., Hensberge, H., et al. 2011, A&A, 526, A69
- Renson, P. & Manfroid, J. 2009, A&A, 498, 961
- Samadi Ghadim, A., Lampens, P., & Jassur, D. M. 2018, Acta Astron., 68, 425
- Samadi-Ghadim, A., Lampens, P., Jassur, D. M., & Jofré, P. 2020, A&A, 638, A57
- Shibahashi, H. & Kurtz, D. W. 2012, MNRAS, 422, 738
- Sikora, J., David-Uraz, A., Chowdhury, S., et al. 2019, MNRAS, 487, 4695
- Uytterhoeven, K., Moya, A., Grigahcène, A., et al. 2011, A&A, 534, A125
- Van Reeth, T., Tkachenko, A., & Aerts, C. 2016, A&A, 593, A120